

A LOW-MASS BLACK HOLE IN THE NEARBY SEYFERT GALAXY UGC 06728

MISTY C. BENTZ¹, MERIDA BATISTE¹, JAMES SEALS¹, KAREN GARCIA¹, RACHEL KUZIO DE NARAY¹, WESLEY PETERS¹,
MATTHEW D. ANDERSON¹, JEREMY JONES¹, KATHRYN LESTER¹, CAMILO MACHUCA¹, J. ROBERT PARKS¹, CRYSTAL L. POPE¹,
MITCHELL REVALSKI¹, CAROLINE A. ROBERTS¹, DICY SAYLOR¹, R. ANDREW SEVRINSKY¹, AND CLAY TURNER¹

(Received; Accepted)
Draft version August 16, 2016

ABSTRACT

We present the results of a recent reverberation mapping campaign for UGC 06728, a nearby low-luminosity Seyfert 1 in a late-type galaxy. Nightly monitoring in the spring of 2015 allowed us to determine an H β time delay of $\tau = 1.4 \pm 0.8$ days. Combined with the width of the variable H β line profile, we determine a black hole mass of $M_{\text{BH}} = (7.1 \pm 4.0) \times 10^5 M_{\odot}$. We also constrain the bulge stellar velocity dispersion from higher-resolution long slit spectroscopy along the galaxy minor axis and find $\sigma_{\star} = 51.6 \pm 4.9 \text{ km s}^{-1}$. The measurements presented here are in good agreement with both the $R_{\text{BLR}} - L$ relationship and the $M_{\text{BH}} - \sigma_{\star}$ relationship for AGNs. Combined with a previously published spin measurement, our mass determination for UGC 06728 makes it the lowest-mass black hole that has been fully characterized, and thus an important object to help anchor the low-mass end of black hole evolutionary models.

Subject headings: galaxies: active — galaxies: nuclei — galaxies: Seyfert

1. INTRODUCTION

Supermassive black holes are now believed to inhabit the nuclei of all massive galaxies. Furthermore, the active galactic nucleus, or AGN, phase is generally understood to be a short-term event in the life of a typical black hole, triggered either by a merger event or secular processes in the host galaxy (cf. the review of Heckman & Best 2014 and references therein). Tight scaling relationships between the observed properties of black holes and their host galaxies point to a symbiotic relationship between the two (e.g., Magorrian et al. 1998; Ferrarese & Merritt 2000; Gebhardt et al. 2000; Gültekin et al. 2009; Kormendy & Ho 2013; van den Bosch 2016), in which the growth of structure and the evolution of galaxies across cosmic time is fundamentally linked to supermassive black holes. Understanding this link requires an understanding of black hole demographics, not just in the local universe, but also at higher redshift where we can witness the growth of structure occurring.

Black holes, as opposed to galaxies, are incredibly simple objects that can be fully characterized with only two fundamental measurements: mass and spin. In the Milky Way, years of astrometric monitoring of stars in the central ~ 0.01 parsec have led to an extremely precise determination of the mass of our own supermassive black hole (Ghez et al. 2000; Genzel et al. 2000; Ghez et al. 2008). Unfortunately, all other galaxies are too distant for this same technique to be employed, and different techniques must be used to understand the masses of a population of central black holes. For galaxies out to ~ 100 Mpc, spatially-resolved observations of the bulk motions of stars or nuclear gas disks can be combined with dynamical modeling to constrain the central black hole mass (cf. the reviews of Ferrarese & Ford 2005; Kormendy & Ho 2013). Reverberation mapping (Blandford & McKee 1982; Peterson 1993), on the other hand, takes advantage of AGN flux variability to constrain black hole masses through time-resolved, rather than spatially-resolved, observations, thus obviating any distance limitations. Furthermore, the most

widely-used technique to constrain supermassive black hole spins requires high X-ray luminosities that are only found in AGNs (e.g., Reynolds 2014 and references therein), so the study of active black holes is an important key to unraveling the growth and evolution of cosmic structure.

Unfortunately, bright AGNs are relatively rare in the local universe, leading to a disconnect in our current understanding of nearby black holes compared to those observed at larger look-back times. In particular, we are lacking direct comparisons of black hole mass constraints through multiple independent techniques in the same galaxies. There are a handful of published comparisons of reverberation masses and gas dynamical masses (e.g., Hicks & Malkan 2008), including the low-mass Seyfert NGC 4395 (Peterson et al. 2005; den Brok et al. 2015). The agreement is generally quite good, although the number of galaxies studied is small. Stellar dynamics, on the other hand, is a good check against reverberation masses because it relies on modeling a non-collisional system, unlike gas dynamics where the AGN may be expected to inject energy on resolvable spatial scales. However, only two such comparisons currently exist for black hole masses from reverberation mapping and stellar dynamical modeling: NGC 4151 (Bentz et al. 2006a; Onken et al. 2014) and NGC 3227 (Denney et al. 2009a; Davies et al. 2006). While the techniques give roughly consistent masses for these two examples, there are caveats and limitations to both reverberation mapping and dynamical modeling, and a larger comparison sample is needed to fully assess the consistency of the local and the cosmological black hole mass scales. We have therefore undertaken a program to identify and monitor local AGNs where it might be possible to obtain both a reverberation and a stellar dynamical mass constraint. Both techniques are time- and resource-intensive, and there are very few broad-lined AGNs within $z \lesssim 0.01$, where the spatial resolution provided by 8–10-m class telescopes would be likely to resolve the black hole’s gravitational influence on the nuclear stellar dynamics, but we hope to increase the sample of mass comparisons by a factor of a few. We currently have stellar dynamical modeling underway for two other local AGNs, and we describe here the reverberation results for an addi-

¹ Department of Physics and Astronomy, Georgia State University, Atlanta, GA 30303, USA; bentz@astro.gsu.edu

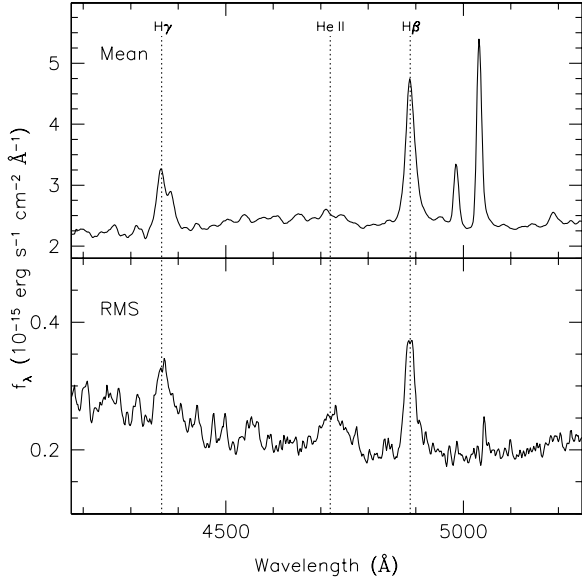


FIG. 1.— Mean (top) and root mean square (bottom) of all the blue-side spectra obtained from APO during the monitoring campaign.

tional local AGN in our sample, UGC 06728.

2. OBSERVATIONS

UGC 06728 is a low-luminosity Seyfert 1 located at $\alpha = 11:45:16.0$, $\delta = +79:40:53$, $z = 0.00652$ in a late-type galaxy that is highly inclined to our line of sight. It was monitored nightly over the course of two months in the spring of 2015. Optical spectroscopy and photometry were obtained at Apache Point Observatory in New Mexico, with additional supporting photometry obtained at Hard Labor Creek Observatory in Georgia. We describe the details below.

2.1. Spectroscopy

Spectrophotometric monitoring of UGC 06728 was carried out at Apache Point Observatory (APO) with the 3.5-m telescope from 2015 April 15 – May 30 (UT dates here and throughout). Our monitoring program was scheduled for the first hour of almost every night during this time period, coincident with evening twilight. We employed the Dual Imaging Spectrograph (DIS), which uses a dichroic to split the incoming beam into a red arm and a blue arm, with the low-resolution (B400/R300) gratings centered at 4398 Å and 7493 Å. The B400 and R300 gratings, when used together, cover the entire optical bandpass between the atmospheric cutoff and 1 μm , with a nominal dispersion of 1.8 Å/pix and 2.3 Å/pix respectively. Spectra were obtained through a 5'' slit rotated to a position angle of 0° (oriented north-south) and centered on the AGN. On each visit, a single spectrum with an exposure time of 600 s was acquired at a typical airmass of 1.5. Observations of the spectrophotometric standard star Feige 34 were also acquired with each visit.

All spectra were reduced with IRAF² following standard procedures. An extraction width of 12 pixels was adopted,

² IRAF is distributed by the National Optical Astronomy Observatory, which is operated by the Association of Universities for Research in Astronomy (AURA) under cooperative agreement with the National Science Foundation.

corresponding to an angular width of 5'' and 4.8'' for the blue and red cameras, respectively.

The desire to minimize sampling gaps and maximize temporal coverage means that ground-based reverberation campaigns must rely on spectroscopy obtained under nonphotometric conditions. While a spectrophotometric standard star can help correct the overall shape of the spectrum for atmospheric effects, as well as those from the telescope and instrument optics, an additional technique is required to achieve absolute flux calibrations of all the spectra. Fortunately, the narrow emission lines do not vary on short timescales of weeks to months, so they can serve as convenient “internal” flux calibration sources. We utilize the van Groningen & Wanders (1992) spectral scaling method, which accounts for small differences in wavelength calibration, flux calibration, and resolution (from variations in the seeing). The method compares each spectrum to a reference spectrum built from the best spectra (identified by the user) and minimizes the differences within a specified wavelength range. The method has been shown to result in relative spectrophotometry that is accurate to $\sim 2\%$ (Peterson et al. 1998a). We restricted the scaling algorithm to focus on the spectral region containing the [O III] $\lambda\lambda 4959, 5007$ doublet. Additionally, we adopted an overall flux scale based on the integrated [O III] $\lambda 5007$ flux measured from the nights with the best observing conditions of $f_{\lambda 5007} = 41.6 \times 10^{-15} \text{ ergs s}^{-1} \text{ cm}^{-2}$. The red-side spectra showed only H α emission smoothly blended with [N II] $\lambda\lambda 6548, 6583$. Emission from [S II] $\lambda\lambda 6716, 6730$ and [O I] $\lambda\lambda 6300, 6363$ is extremely weak and difficult to detect above the continuum. With no suitable narrow lines available, we were unable to accurately intercalibrate the red-side spectra and we do not consider them further.

Figure 1 displays the final mean and root mean square (rms) of all the calibrated spectra acquired throughout the campaign. The rms spectrum displays the variable spectral components, of which H β , He II $\lambda 4686$, and H γ are apparent, as is the AGN continuum.

2.2. Photometry

Broad-band g and r images were obtained at APO with the imaging mode of the DIS spectrograph each night directly after acquiring the spectra. The dual-arm nature of the spectrograph allowed both images to be obtained simultaneously. The typical exposure time was 30 s, and a single image in each filter was obtained per visit. Images were reduced in IRAF following standard procedures. The DIS imaging mode provides a relatively small field of view ($\sim 4' \times 7'$), but there were a handful of convenient bright stars in all of the images (see Figure 2). We carried out aperture photometry employing circular apertures with radii of $3''.78$ in g and $3''.6$ in r , and sky annuli of $6''.3\text{--}7''.56$ and $6''.0\text{--}7''.2$ respectively. Calibrated g - and r -band magnitudes for three field stars were adopted from APASS (the AAVSO Photometric All Sky Survey; Henden & Munari 2014) and set the photometric zero-points.

Photometric monitoring was also carried out with the 24-inch Miller Telescope at Hard Labor Creek Observatory (HLCO), owned and operated by Georgia State University in Hard Labor Creek State Park near Rutledge, GA. V-band images were acquired with an Apogee 2048 \times 2048 detector, spanning a field of view of $26'.3 \times 26'.3$ with a pixel scale of $0''.77$. On a typical night, three exposures were obtained at an airmass of ~ 1.5 , each with an exposure time of 300 s.

The wide field of view of the HLCO images included a large

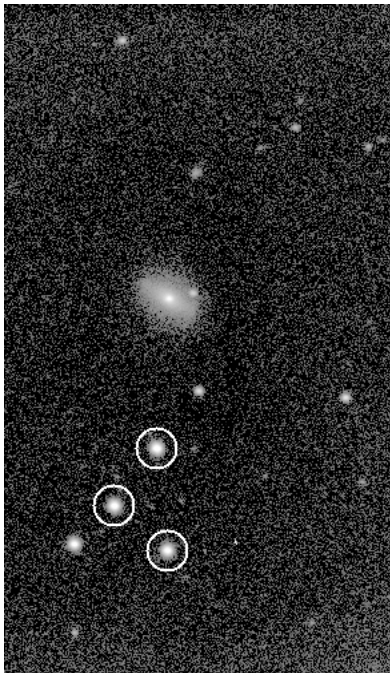


FIG. 2.— Example r -band image acquired with the imaging mode of the DIS spectrograph at APO. The field stars used to set the magnitude zeropoint are marked with circles. The scale of the image is $3'.9 \times 6'.7$ and is oriented with north up and east to the right.

number of field stars, allowing us to derive a V -band light curve for UGC 06728 by employing image subtraction techniques. We first registered all the images to a common alignment with the *Sexterp* package (Siverd et al. 2012). We then carried out the image subtraction analysis with the *ISIS* package (Alard & Lupton 1998; Alard 2000). *ISIS* builds a reference frame from the best images (specified by the user) and then uses a spatially-varying kernel to convolve the reference frame to match each individual image in the dataset. Subtraction of the two results in a residual image in which all constant components have disappeared and only variable flux remains. In the case of UGC 06728, the host-galaxy and the average AGN brightness are subtracted from all the residual images, leaving behind only the brightness of the AGN relative to its mean level. Aperture photometry is then employed to measure this variable flux, which may be positive or negative, at the location of the target of interest in each residual image, providing a V -band residual light curve.

3. LIGHT CURVE ANALYSIS

Light curves for the broad emission lines $H\beta$, $\text{He II } \lambda 4686$, and $H\gamma$ were derived directly from the scaled spectra. We fit a local, linear continuum below each emission line and then integrated the flux above this continuum to determine the total emission-line flux. This includes the contribution from the narrow component of each emission line, which is simply a constant flux offset. We also determined a continuum light curve from the spectra at $5100 \times (1+z) \text{ \AA}$, which has the merit of being completely uncontaminated by emission lines. The strong continuum and emission-line variability over the course of the campaign allows us to determine these light curves directly from the spectra without carrying out any spectral modeling or decomposition, which has the potential to introduce artificial features into light curves.

In Figure 3, we show the spectroscopic continuum light

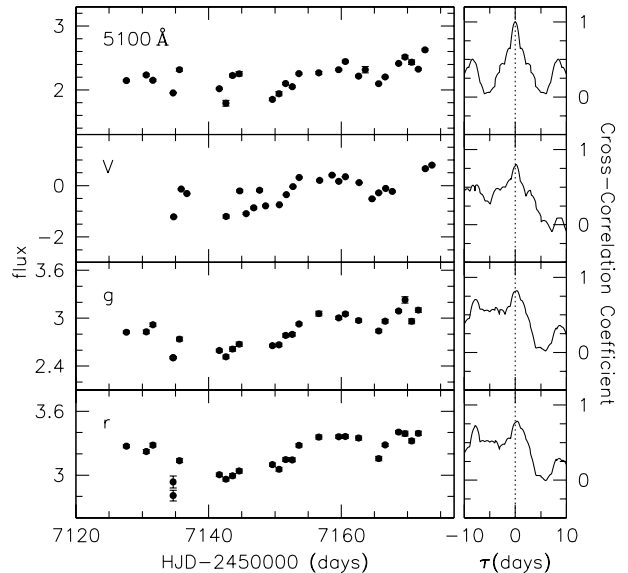


FIG. 3.— Spectroscopic continuum and photometric light curves (*left panels*) and the cross-correlation of each light curve relative to the spectroscopic continuum light curve (*right panels*). No apparent time delays are detected, except perhaps in the r band, and the light curve features are quite similar.

curve relative to the V -band residual light curve and the g and r photometric light curves (tabulated in Table 1). The V -band residual light curve does not contain significant emission from any broad emission lines, so we combined it with the continuum light curve determined from our spectra to improve the time sampling, especially in the first half of the campaign. We selected pairs of points from the two light curves that were contemporaneous within 0.5 days and fit for the best multiplicative and additive factors to bring the V -band residual fluxes into agreement with the measured continuum flux densities. These best-fit factors account for the differences in host-galaxy background light, average AGN flux level, and bandpass. The V -band light curve was scaled according to the best-fit parameters and merged with the continuum light curve. We then examined the g -band light curve from the APO photometry and found that there was no significant time delay relative to the merged continuum+ V light curve, so we merged it as well by again finding the multiplicative and additive scale factors necessary to bring it into agreement with contemporaneous points in the continuum+ V light curve. Our final merged continuum light curve was binned to 0.5 day sampling to improve the accuracy. The overall shape of the r -band light curve agrees with the other photometric light curves and the continuum light curve, but the variability level is somewhat damped by additional host-galaxy flux and there is possibly a slight delay in the light curve, so we did not merge the r -band with the other light curves. A detectable delay in r is not unexpected, given that the filter bandpass is centered on $H\alpha$. While g is centered on $H\beta$, the overall contribution of $H\beta$ to the total filter bandpass is much smaller than for $H\alpha$ and r . In particular, $H\beta$ contributes only 2% of the g -band flux, with the variable component of $H\beta$ accounting for only 10% of the total $H\beta$ contribution, or 0.2% of the total g -band flux. On the other hand, $H\alpha$ contributes 15% of the total r -band flux.

Figure 4 displays the final merged and binned continuum light curve and the broad emission-line light curves (tabulated

TABLE 1
PHOTOMETRIC LIGHT CURVES

HJD (days)	g (AB mag)	r (AB mag)	HJD (days)	V (resid. cts/10000)
7127.6059	15.546 ± 0.006	14.823 ± 0.005	7134.7311	1.216 ± 0.024
7130.6023	15.544 ± 0.008	14.840 ± 0.006	7135.8689	0.133 ± 0.025
7131.6043	15.510 ± 0.008	14.820 ± 0.006	7136.7193	0.309 ± 0.024
7134.6484	15.676 ± 0.006	14.941 ± 0.021	7142.6382	1.202 ± 0.060
7134.6493	15.677 ± 0.005	14.989 ± 0.020	7144.6886	0.205 ± 0.042
7135.6058	15.580 ± 0.009	14.869 ± 0.006	7145.6625	1.093 ± 0.034
7141.6148	15.638 ± 0.007	14.916 ± 0.006	7146.8040	0.865 ± 0.038
7142.6108	15.671 ± 0.010	14.931 ± 0.007	7147.6872	0.180 ± 0.045
7143.6100	15.630 ± 0.011	14.919 ± 0.007	7148.5865	0.789 ± 0.021
7144.6099	15.605 ± 0.011	14.903 ± 0.007	7150.6653	0.746 ± 0.024
7149.6224	15.612 ± 0.006	14.882 ± 0.005	7151.7214	0.351 ± 0.026
7150.6151	15.608 ± 0.009	14.898 ± 0.006	7152.7171	0.036 ± 0.020
7151.6161	15.561 ± 0.008	14.866 ± 0.006	7153.6520	-0.319 ± 0.022
7152.6159	15.556 ± 0.008	14.867 ± 0.006	7156.7405	-0.204 ± 0.042
7153.6223	15.507 ± 0.006	14.820 ± 0.005	7158.6132	-0.410 ± 0.025
7156.6189	15.460 ± 0.010	14.795 ± 0.006	7159.6255	-0.170 ± 0.026
7159.6214	15.479 ± 0.007	14.794 ± 0.005	7160.6317	-0.346 ± 0.009
7160.6215	15.461 ± 0.007	14.793 ± 0.005	7162.6928	-0.118 ± 0.021
7162.6218	15.491 ± 0.007	14.798 ± 0.006	7164.6410	0.514 ± 0.025
7165.6511	15.540 ± 0.008	14.862 ± 0.007	7165.6504	0.280 ± 0.025
7166.6239	15.494 ± 0.008	14.819 ± 0.005	7166.7008	0.109 ± 0.024
7168.6555	15.448 ± 0.005	14.780 ± 0.005	7167.7025	0.226 ± 0.021
7169.6224	15.400 ± 0.014	14.785 ± 0.007	7172.6709	-0.661 ± 0.037
7170.6218	15.495 ± 0.011	14.807 ± 0.006	7173.6752	-0.801 ± 0.030
7171.6249	15.444 ± 0.009	14.784 ± 0.006		

TABLE 2
SPECTROSCOPIC LIGHT CURVES

HJD (days)	$5100 \times (1+z) \text{ \AA}$ ($10^{-15} \text{ erg s}^{-1} \text{ cm}^{-2} \text{ \AA}^{-1}$)	H β ($10^{-15} \text{ erg s}^{-1} \text{ cm}^{-2}$)	H γ ($10^{-15} \text{ erg s}^{-1} \text{ cm}^{-2}$)	He II ($10^{-15} \text{ erg s}^{-1} \text{ cm}^{-2}$)
7127.60131629	2.146 ± 0.013	76.605 ± 0.039	45.467 ± 0.091	12.614 ± 0.092
7130.59772753	2.235 ± 0.018	65.745 ± 0.064	31.085 ± 0.126	7.226 ± 0.158
7131.59975985	2.151 ± 0.016	66.059 ± 0.053	34.986 ± 0.098	11.465 ± 0.127
7134.64244313	1.953 ± 0.007	59.745 ± 0.009	29.567 ± 0.011	8.501 ± 0.014
7135.60113042	2.317 ± 0.023	60.694 ± 0.101	30.367 ± 0.206	5.223 ± 0.263
7141.6102368	2.019 ± 0.011	55.835 ± 0.025	27.859 ± 0.045	3.583 ± 0.056
7142.60623451	1.792 ± 0.045	54.629 ± 0.464	31.498 ± 1.061	7.873 ± 1.207
7143.6053809	2.227 ± 0.023	55.439 ± 0.101	31.572 ± 0.221	2.160 ± 0.262
7144.60529841	2.253 ± 0.033	58.688 ± 0.236	26.036 ± 0.502	...
7149.61781551	1.852 ± 0.021	56.921 ± 0.089	31.359 ± 0.145	4.714 ± 0.176
7150.61051989	1.941 ± 0.031	53.080 ± 0.185	25.462 ± 0.354	8.538 ± 0.455
7151.61149262	2.101 ± 0.016	60.457 ± 0.054	36.374 ± 0.109	8.983 ± 0.131
7152.61133458	2.051 ± 0.016	57.825 ± 0.050	34.132 ± 0.107	12.753 ± 0.123
7153.61769047	2.256 ± 0.011	63.765 ± 0.025	32.758 ± 0.042	19.423 ± 0.055
7156.61430815	2.268 ± 0.021	63.760 ± 0.086	38.456 ± 0.175	1.949 ± 0.212
7159.61682615	2.317 ± 0.013	67.404 ± 0.033	34.757 ± 0.066	14.462 ± 0.080
7160.61690956	2.445 ± 0.019	73.758 ± 0.067	31.379 ± 0.128	19.432 ± 0.164
7162.61714264	2.216 ± 0.013	72.343 ± 0.031	37.067 ± 0.058	15.755 ± 0.076
7163.62052311	2.317 ± 0.051	65.958 ± 0.505	32.747 ± 1.106	11.655 ± 1.309
7165.63733328	2.098 ± 0.010	64.085 ± 0.019	32.687 ± 0.026	9.924 ± 0.032
7166.61939046	2.203 ± 0.013	70.381 ± 0.032	35.662 ± 0.059	10.006 ± 0.076
7168.65095798	2.415 ± 0.008	66.380 ± 0.012	35.326 ± 0.015	15.805 ± 0.019
7169.61788092	2.515 ± 0.026	67.836 ± 0.125	35.631 ± 0.273	14.877 ± 0.332
7170.61722538	2.434 ± 0.037	76.008 ± 0.228	36.909 ± 0.465	19.810 ± 0.575
7171.62035657	2.325 ± 0.014	66.832 ± 0.036	42.273 ± 0.072	13.417 ± 0.088
7172.62633782	2.627 ± 0.014	72.460 ± 0.035	39.271 ± 0.062	22.804 ± 0.080

in Table 2. The variability statistics for each of the light curves are tabulated in Table 3. Column (1) lists the spectral feature and column (2) gives the number of measurements in the light curve. Columns (3) and (4) list the average and median time separation between measurements, respectively. Column (5) gives the mean flux and standard deviation of the light curve, and column (6) lists the mean fractional error (based on the comparison of observations that are closely spaced in time).

Column (7) lists the excess variance, computed as:

$$F_{\text{var}} = \frac{\sqrt{\sigma^2 - \delta^2}}{\langle F \rangle} \quad (1)$$

where σ^2 is the variance of the fluxes, δ^2 is their mean-square uncertainty, and $\langle F \rangle$ is the mean flux. And column (8) is the ratio of the maximum to the minimum flux in the light curve, R_{max} .

TABLE 3
LIGHT-CURVE STATISTICS

Time Series	N	$\langle T \rangle$ (days)	T_{median} (days)	$\langle F \rangle^a$	$\langle \sigma_F / F \rangle$	F_{var}	R_{max}
5100 Å	26	1.8 ± 1.4	1.0	2.21 ± 0.20	0.009	0.090	1.466 ± 0.038
V	24	1.7 ± 1.3	1.1	-0.22 ± 0.56	0.050	-2.56	-0.659 ± 0.028
g	25	1.8 ± 1.4	1.0	2.83 ± 0.21	0.008	0.072	1.290 ± 0.017
r	25	1.8 ± 1.4	1.0	3.19 ± 0.17	0.007	0.052	1.213 ± 0.023
H β	26	1.8 ± 1.4	1.0	64.3 ± 6.7	0.002	0.105	1.443 ± 0.005
H γ	26	1.8 ± 1.4	1.0	33.9 ± 4.6	0.007	0.135	1.786 ± 0.025
He II	25	1.9 ± 1.5	1.0	11.3 ± 5.7	0.033	0.500	11.7 ± 1.3

^a 5100 Å, g -band, and r -band flux densities are in units of $10^{-15} \text{ ergs s}^{-1} \text{ cm}^{-2} \text{ Å}^{-1}$. V-band residual flux is in units of 10000 counts. Emission line fluxes are in units of $10^{-15} \text{ ergs s}^{-1} \text{ cm}^{-2}$.

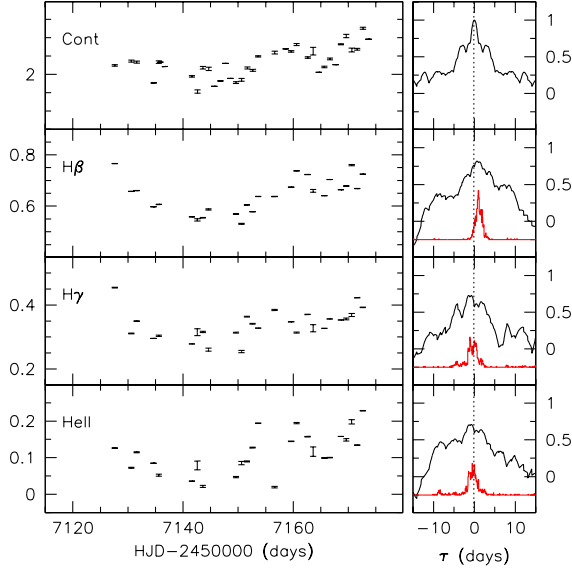


FIG. 4.— Merged continuum light curve and emission-line light curves (*left panels*). The right panels display the cross-correlation of each light curve relative to the continuum, and the red histograms (arbitrarily scaled) display the cross-correlation centroid distributions.

We employed the interpolated cross-correlation function (ICCF) methodology (Gaskell & Sparke 1986; Gaskell & Peterson 1987) with the modifications of White & Peterson (1994) to search for time delays of the emission lines relative to the continuum. The ICCF method calculates the cross-correlation function (CCF) twice, by interpolating first one light curve and then the other, and averages the two results together to determine the final CCF. The CCF can be characterized by its maximum value (r_{max}), the time delay at which the maximum occurs (τ_{peak}) and the centroid (τ_{cent}) of the points around the peak above some value (typically $0.8r_{\text{max}}$). CCFs for each light curve relative to the continuum are displayed in Figure 4 (*right panels*). For the continuum light curve, this is the autocorrelation function.

To quantify the uncertainties on the time delay measurements, τ_{cent} and τ_{peak} , we employ the Monte Carlo “flux randomization/random subset sampling” method of Peterson et al. (1998b, 2004). This method is able to account for the measurement uncertainties as well as the effect of including or excluding any particular data point. The “random subset sampling” is implemented such that, from the N available data points within a light curve, N points are selected without regard to whether a point has been previously chosen.

For a point that is sampled $1 \leq n \leq N$ times, the uncertainty on that point is scaled by a factor of $n^{1/2}$. The typical number of points that is not selected in any specific realization is $\sim 1/e$. The “flux randomization” component takes the newly sampled light curve and modifies the flux values by a Gaussian deviation of the flux uncertainty. These modified light curves are then cross-correlated with the ICCF method described above, and the whole process is repeated many times ($N = 1000$). From the large set of realizations, we build distributions of τ_{cent} and τ_{peak} . The median of each distribution is taken to be the measurement value, and the uncertainties are set such that they mark the upper 15.87% and lower 15.87% of the realizations (corresponding to $\pm 1\sigma$ for a Gaussian distribution). The red histograms in the Figure 4 depict the cross-correlation centroid distribution for each emission line.

To further check that combining the various photometric and spectroscopic light curves has not affected our measured time delays, we also determined the time delay of H β relative to each of the individual continuum, V-band, and g -band light curves. Each of these light curves is slightly undersampled relative to the combined continuum light curve, but the CCFs and recovered H β time delays agree within the measurement uncertainties.

We also investigated the time delays with the JAVELIN package (Zu et al. 2011). JAVELIN fits the continuum variations with a damped random walk model. It then assumes a top hat model for the reprocessing function, and determines the best-fit shifting and smoothing parameters for the emission-line light curves by maximizing the likelihood of the model. Uncertainties on each of the model parameters are assessed through a Bayesian Markov Chain Monte Carlo method. We denote time delays from JAVELIN as τ_{jav} . Given the extremely short time delays, we were unable to fit a single model while including all the emission lines simultaneously, so we instead modeled each emission line separately relative to the continuum (see Figure 5).

Time delay measurements are listed in Table 4. While each of the measurements is an observed time delay, the rest-frame time delays, corrected for a factor of $1+z$, are formally the same within the uncertainties.

4. LINE WIDTH MEASUREMENTS

The widths of the broad emission lines in AGN spectra are interpreted as the line-of-sight velocities of the bulk motion of the gas. The narrow emission lines, however, are known to emit from gas that is not participating in the same bulk motion. Therefore, good practice is to isolate the broad emission from the narrow emission when quantifying the line width. In the spectrum of UGC 06728, however, it is not clear what part

TABLE 4
TIME LAGS

Feature	τ_{cent} (days)	τ_{peak} (days)	τ_{jav} (days)
H β	$1.4^{+0.7}_{-0.8}$	$1.1^{+0.6}_{-0.6}$	$1.3^{+0.2}_{-0.7}$
H γ	$0.0^{+1.0}_{-1.3}$	$-0.7^{+2.5}_{-0.7}$	$-1.5^{+0.1}_{-0.7}$
He II	$-0.2^{+0.9}_{-1.1}$	$-0.7^{+1.8}_{-0.7}$	$-1.4^{+0.2}_{-0.1}$

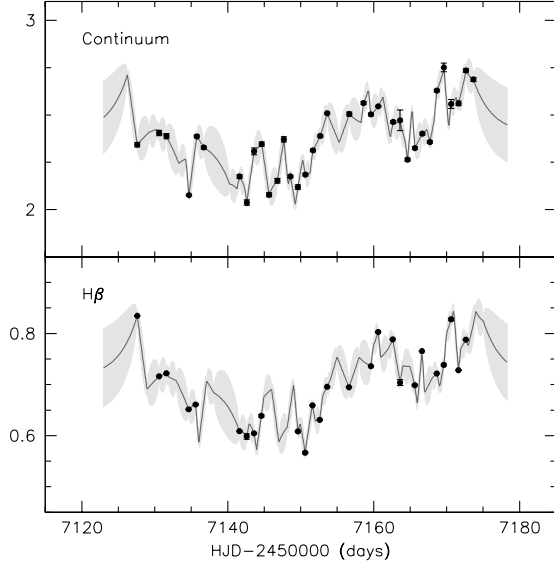


FIG. 5.— Continuum and H β light curves with interpolated JAVELIN light curves drawn from the distribution of acceptable models.

of the H β line is narrow emission (cf. Figure 1). Furthermore, the narrow lines contribute almost no signal to the rms spectrum, demonstrating that our internal spectral scaling method has minimized their apparent variability from changing observing conditions throughout the monitoring campaign. As it is the variable part of the emission line (the rms profile) that we are most interested in, we do not attempt any narrow line subtraction for this object.

We measured the widths of the broad H β , He II λ 4686, and H γ emission lines in both the mean and the rms spectra and we report two different line width characterizations: the full width at half the maximum flux (FWHM) and the second moment of the line profile (σ_{line}). Line widths were measured directly from the spectra, with each line profile defined as the flux above a local linear continuum. Uncertainties in the emission line widths were determined using a Monte Carlo random subset sampling method. From a set of N spectra, a subset of N spectra were selected without regard to whether they had been previously chosen. The mean and rms of the subset were created, from which the FWHM and σ_{line} of an emission line were determined and recorded. Distributions of line width measurements were built up over 1000 realizations. We take the mean and the standard deviation of each distribution as the measurement and its uncertainty, respectively.

Following Peterson et al. (2004), we corrected the emission-line widths for the dispersion of the spectrograph. The observed emission line width, $\Delta\lambda_{\text{obs}}$, can be described as

$$\Delta\lambda_{\text{obs}}^2 \approx \Delta\lambda_{\text{true}}^2 + \Delta\lambda_{\text{disp}}^2 \quad (2)$$

where $\Delta\lambda_{\text{true}}$ is the intrinsic line width and $\Delta\lambda_{\text{disp}}$ is the broadening induced by the spectrograph. The employment of a wide spectrograph slit for reverberation campaigns means that the spectrograph dispersion cannot be determined from night sky emission lines or from arc lamp lines — the unresolved AGN point source, even under poor seeing conditions, will not fill the spectrograph slit. Given the relative obscurity of this particular AGN, we were unable to estimate $\Delta\lambda_{\text{true}}$, and therefore constrain $\Delta\lambda_{\text{disp}}$, from high-quality, high-resolution observations of the narrow emission lines in the literature. However, we have previously monitored other AGNs with this same instrumental setup, and so we adopt the value of $\Delta\lambda_{\text{disp}} = 14.1 \text{ \AA}$ that we determined for NGC 5273 from a spring 2014 monitoring campaign (Bentz et al. 2014).

Our final resolution-corrected line width measurements are listed in Table 5.

5. BLACK HOLE MASS

All of the time delays measured for UGC 06728 are very short, which is to be expected given the low luminosity of the AGN. The time delays determined for H β are the only ones that are not formally consistent with zero within the measurement uncertainties, so H β is the only emission line we will consider for the determination of the black hole mass. However, H β is also the emission line for which we have the largest number of reverberation results (cf. Bentz & Katz 2015 for a recent summary), so it is also the most reliable emission line for determining M_{BH} .

The black hole mass is generally determined from reverberation-mapping measurements as:

$$M_{\text{BH}} = f \frac{c\tau V^2}{G} \quad (3)$$

where τ is the time delay for a specific emission line relative to variations in the continuum, and V is the line-of-sight velocity width of the emission line, with c and G being the speed of light and gravitational constants, respectively. The emission-line time delay is interpreted as a measure of the responsivity-weighted average radius of the broad-line region for that specific emission feature (e.g., H β).

The scaling factor f accounts for the detailed geometry and kinematics of the broad line region gas, which is unresolved. In practice, the multiplicative factor, $\langle f \rangle$, which is found to bring the $M_{\text{BH}} - \sigma_*$ relationship for AGNs with reverberation masses into agreement with the $M_{\text{BH}} - \sigma_*$ relationship for nearby galaxies with dynamical black hole masses (e.g., Gültekin et al. 2009; McConnell & Ma 2013; Kormendy & Ho 2013) is used as a proxy for f . In this way, the population average factor provides an overall scale for reverberation masses that should be unbiased, but the mass of any particular AGN is expected to be uncertain by a factor of 2-3 because of object-to-object variations. The value of $\langle f \rangle$ has varied in the literature from 5.5 (Onken et al. 2004) to 2.8 (Graham et al. 2011), depending on which objects are included and the specifics of the measurements. We adopt the value determined by Grier et al. (2013) of $\langle f \rangle = 4.3 \pm 1.1$.

Combining the time lag (τ_{cent}) and line width (σ_{line}) measurements for H β and scaling by $\langle f \rangle$, we determine $M_{\text{BH}} = (7.1 \pm 4.0) \times 10^5 M_{\odot}$.

6. DISCUSSION

The extremely rapid response of the broad emission lines to variations in the continuum flux in UGC 06728 means that

TABLE 5
LINE WIDTHS

Feature	Mean		RMS	
	FWHM (km s ⁻¹)	σ_{line} (km s ⁻¹)	FWHM (km s ⁻¹)	σ_{line} (km s ⁻¹)
H β	1144.5 \pm 58.3	758.3 \pm 19.4	1309.7 \pm 182.2	783.7 \pm 92.3
H γ	2333.6 \pm 80.3	821.8 \pm 21.8	2492.3 \pm 1704.7	919.9 \pm 70.4
He II	2626.2 \pm 593.7	1124.7 \pm 127.7	4016.7 \pm 912.9	1605.6 \pm 157.8

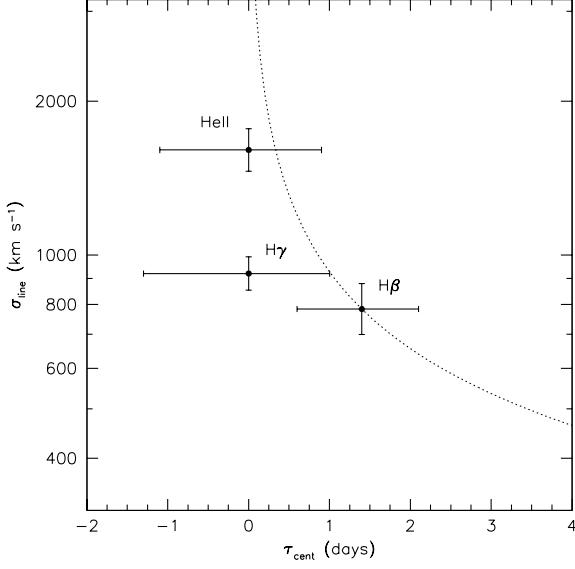


FIG. 6.— Line width versus time delay as measured from the broad optical recombination lines in the spectrum of UGC 06728. The dotted line shows the expected relationship of $R \propto V^{-2}$ and is scaled to match the measurements for H β . Even though the time delays are quite short, and unresolved in the case of H γ and He II, the measurements are in relatively good agreement with the expected relationship.

our daily sampling was not fine enough to resolve time delays for all the broad optical recombination lines. The time delay of H β is the only one that is not formally consistent with zero delay, and it is only marginally resolved at that. However, while we were not able to resolve the time delays for H γ and He II, we can examine them in light of the expected virial relationship for BLR gas that is under the gravitational dominance of the black hole. In particular, we would expect that $R \propto V^{-2}$. This relationship has been shown to be a good description of observations when reverberation results from multiple emission lines have been recovered (e.g., Peterson et al. 2004; Kollatschny 2003; Bentz et al. 2010). Figure 6 shows the measurements for the optical recombination lines in UGC 06728, with the expected relationship scaled to match the measurements for H β . There is generally good agreement with the expected relationship within the measurement uncertainties, such that we would not expect to resolve the responses of these emission lines with our current sampling. A monitoring campaign with finer temporal resolution ($\Delta t = 0.25\text{--}0.5$ days) would be needed to further improve upon these constraints.

6.1. Consistency with the $R_{\text{BLR}} - L$ Relationship

Furthermore, we can examine the location of UGC 06728 on the AGN $R_{\text{BLR}} - L$ relationship to further assess the H β

time delay measurement. For very nearby galaxies like UGC 06728, however, one complication is the large fraction of host-galaxy starlight that contributes to the continuum emission at rest-frame 5100 Å through the large spectroscopic slit ($\sim 5''$) employed in a reverberation mapping campaign. The usual method to correct for this contamination is to carry out two-dimensional surface brightness modeling of a high-resolution image of the galaxy (usually from the *Hubble Space Telescope* to maximize the image quality), thereby isolating the host-galaxy starlight components from the unresolved AGN point source. Using the modeling results to create an “AGN-free” image allows the starlight contribution to be directly constrained (Bentz et al. 2006b, 2009, 2013). Unfortunately, there are no *HST* images of UGC 06728. The highest resolution optical images available are the APO DIS *g*-band images discussed above, with a pixel scale of 0.42''/pixel. While hardly comparable to the quality afforded by *HST*, the DIS images do allow us to place some rough constraints on the starlight contribution to the flux density at $5100 \times (1+z)$ Å.

We aligned and stacked several of the *g*-band images to increase the signal-to-noise in the combined image. Using the two-dimensional surface brightness fitting program GALFIT (Peng et al. 2002, 2010), we created a model of the point spread function (PSF) of the stacked image by fitting multiple Gaussian components to the profile of a field star in a restricted portion of the image. We then employed this model PSF while fitting the full frame, including a background sky gradient, a PSF for the AGN and the nearby star, an exponential profile for the disk of the galaxy, and a Sérsic profile for the bulge. The bulge profile, in particular, is very compact with a half-light radius of 1.7 pix (0.7''), and likely degenerate with the AGN PSF, so we caution that our estimate of the starlight contribution is probably more like a lower limit. Figure 7 displays a 2.5×2.5 region of the stacked *g*-band image, our best-fit model from GALFIT, and the residuals after subtracting the model from the image.

As described earlier, calibrated *g*-band photometry for three field stars from APASS (the AAVSO Photometric All Sky Survey; Henden & Munari 2014) was used to set the overall flux scale of the image. We also account for a slight flux scaling factor, due to the difference in effective wavelength of the *g* filter compared to $5100 \times (1+z)$ Å, using Synphot and a template galaxy bulge spectrum (Kinney et al. 1996). Our estimate of the host-galaxy contribution to the spectroscopic flux density is $f_{\text{gal}} = (1.09 \pm 0.22) \times 10^{-15} \text{ ergs s}^{-1} \text{ cm}^{-2} \text{ Å}^{-1}$. Removing this contribution results in an AGN-only continuum flux density of $f_{\text{AGN}} = (1.12 \pm 0.23) \times 10^{-15} \text{ ergs s}^{-1} \text{ cm}^{-2} \text{ Å}^{-1}$. Assuming a luminosity distance of $D_L = 27 \text{ Mpc}$ and correcting for Galactic absorption along the line of sight (Schlafly & Finkbeiner 2011), we derive $\log \lambda L_\lambda = 41.83 \pm 0.24 \text{ ergs s}^{-1}$.

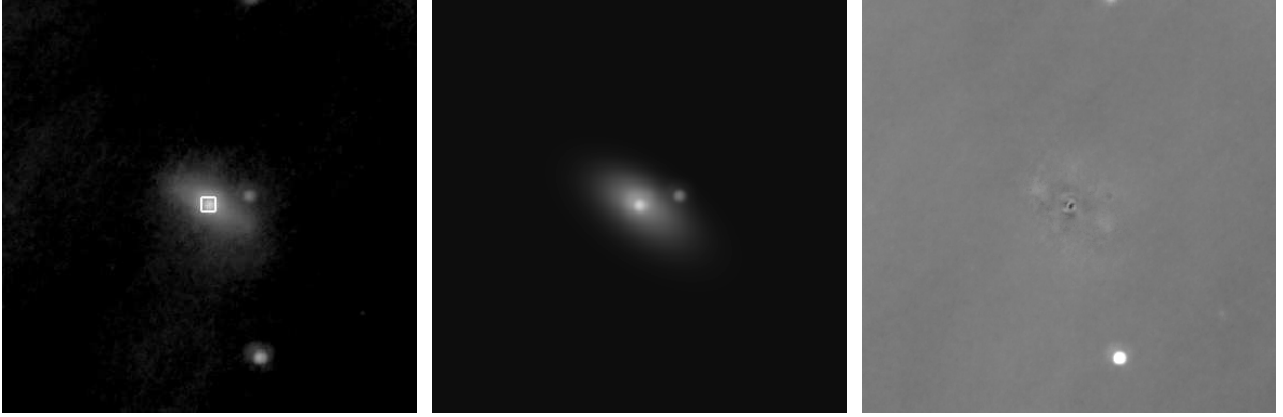


FIG. 7.— Stacked g -band image of a $2''.5 \times 2''.5$ region centered on UGC 06728 (*left*) with the white rectangle showing the geometry of the ground-based spectroscopic monitoring aperture. The best-fit model determined from GALFIT is displayed in the middle panel, and the right panel shows the residuals after subtraction of the model from the image. All images are oriented with north up and east to the right.

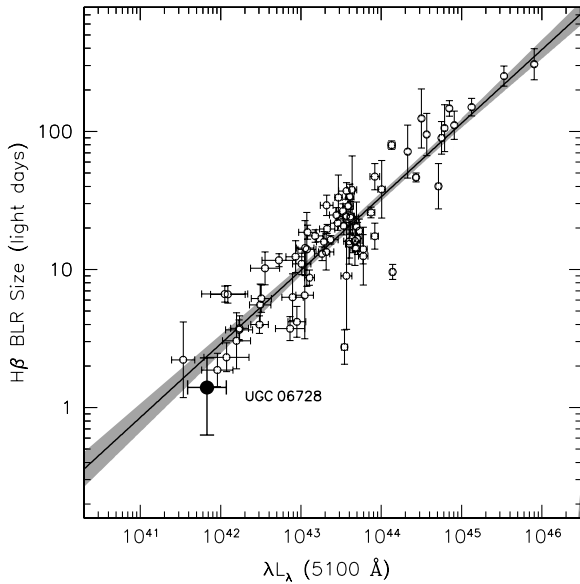


FIG. 8.— The $H\beta$ time delay for UGC 06728 and estimated AGN luminosity (filled point) compared to the radius-luminosity relationship for other reverberation-mapped AGNs (Bentz et al. 2013).

Figure 8 displays the $R_{\text{BLR}}-L$ relationship for nearby AGNs based on reverberation mapping of $H\beta$ (Bentz et al. 2013). The filled circle shows the location of UGC 06728 with the $H\beta$ time delay we have derived here and the luminosity after correction for the estimated starlight contribution. The agreement between UGC 06728 and its expected location based on its estimated luminosity is extremely good considering the barely-resolved nature of the time delay and the caveats in the luminosity determination. Furthermore, we can expect that the agreement is actually somewhat better than depicted, given the likelihood that the starlight correction to the luminosity is underestimated as described above.

Taking our galaxy decomposition at face value, we can estimate the bulge-to-total ratio as $B/T \approx 0.2$, which suggests that the Hubble type of the galaxy is $\sim \text{Sb}$ (Kent 1985). We also estimate the color of the galaxy as $g-r \approx 0.9$, which suggests $M/L_g \approx 6$ (Zibetti et al. 2009). The total stellar mass of the galaxy is $M_* \approx 7.5 \times 10^9 M_\odot$, which also agrees with the host-galaxy being Sb–Sc in type.

6.2. Consistency with the $M_{\text{BH}}-\sigma_*$ Relationship

To further explore the reverberation results for UGC 06728 within the context of the larger reverberation sample, we obtained supplemental observations on 2016 May 13 with the DIS Spectrograph on the APO 3.5-m telescope with the intent of constraining the bulge stellar velocity dispersion. The high resolution B1200 and R1200 gratings were employed, providing nominal dispersions of 0.62 \AA/pix and 0.58 \AA/pix and wavelength coverages of 1240 \AA and 1160 \AA , respectively. The blue grating was centered at 4900 \AA to target the Mgb stellar absorption signature, and the red grating was centered at 8500 \AA for the Ca II triplet absorption. The $0''.9$ slit was rotated to a position angle of 150° east of north, approximately along the minor axis of the galaxy. Given the high inclination of the galaxy, we specifically avoided the major axis of the galaxy to mitigate the effects of rotational broadening from the disk within the one-dimensional extracted spectra. Two 1200 s exposures were obtained through patchy clouds and with marginal seeing at an airmass of 1.6. Spectra of the standard star, Feige 34, were also obtained to assist with the flux calibration, as well as spectra of HD 125560 (spectral type K3III) and HD 117876 (spectral type G8III) to provide velocity templates with the same wavelength coverage and dispersion as the galaxy. All spectra were reduced with IRAF following standard procedures. An extraction width of 40 pixels (corresponding to $16''$ on the blue camera and $16.8''$ on the red camera) was adopted to maximize the galaxy signal in the resultant spectra.

Following flux calibration of the spectra, we employed the pPXF (Penalized Pixel Fitting) method of Cappellari & Emsellem (2004) to extract the stellar kinematics. The Mgb absorption signature was not detected in the galaxy spectra, but the Ca II triplet features were detected, so we focused on fitting the red spectra only. During the fitting process, we restricted the wavelength region to $8525\text{--}8850 \text{ \AA}$ and determined the best-fit parameters (velocity, velocity dispersion, $h3$, and $h4$) using first one velocity template star and then the other. The best fits to the spectrum of UGC 06728 are displayed in Figure 9: HD125560 (red line) provided a best-fit velocity dispersion of 56.5 km s^{-1} , and HD117876 (blue line) provided a best fit of 46.7 km s^{-1} . We take the average of these as the bulge stellar velocity dispersion, $\sigma_* = 51.6 \pm 4.9 \text{ km s}^{-1}$.

With this constraint on the bulge stellar velocity dispersion in UGC 06728, we can explore its location on the AGN $M_{\text{BH}}-$

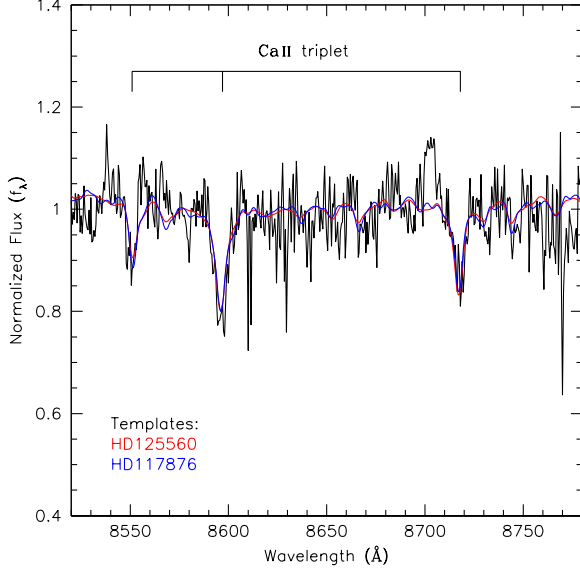


FIG. 9.— Spectrum of UGC 06728 in the wavelength region around the Ca II triplet absorption lines. The red and blue lines show the best-fit models to the stellar absorption lines based on HD125560 and HD117876, respectively. We take the average of the solutions provided by the two template stars as our measurement of the bulge stellar velocity dispersion in UGC 06728.

σ_* relationship. Figure 10 displays the AGN $M_{\text{BH}} - \sigma_*$ relationship from Grier et al. (2013) (open points and line), with the location of UGC 06728 shown by the filled circle. The scatter at the low-mass end of the $M_{\text{BH}} - \sigma_*$ relationship for AGNs with reverberation masses seems to be much smaller than that found for megamaser host galaxies (Greene et al. 2010). Läscher et al. (2016) also found the megamaser host galaxies to have a high scatter relative to the $M_{\text{BH}} - L_{\text{bulge}}$ and $M_{\text{BH}} - M_{\text{bulge}}$ relationships. Each sample of direct black hole masses, whether dynamical, reverberation, or masering, has its own set of biases and assumptions that are independent of the other techniques, so further exploration into this apparent disagreement is likely to shed light on the reliability of black hole mass measurements as they are currently applied.

Furthermore, we can estimate the black hole sphere of influence (r_h) in the nucleus of UGC 06728. Generally defined as

$$r_h = \frac{GM_{\text{BH}}}{\sigma_*^2}, \quad (4)$$

r_h is often employed as a convenient metric for determining the probability of success for constraining M_{BH} from spatially resolved stellar dynamics. Gültekin et al. (2009) argue that a strict reliance on resolving r_h is not necessary, however, for useful constraints on black hole masses.

Combining our measurements of M_{BH} and σ_* and again assuming a luminosity distance of $D_L = 27$ Mpc, we estimate $r_h = 0.01''$ for UGC 06728. While this angular size is smaller than the achievable spatial resolution of integral field spectrographs on the largest ground-based telescopes today, it is interesting to note that it is not much smaller than r_h for NGC 3227. Davies et al. (2006) were able to constrain the black hole mass of NGC 3227 through stellar dynamical modeling, even though the reverberation mass and bulge stellar velocity dispersion predict $r_h = 0.018''$. Given the very limited number of AGNs where it will be possible to carry out a direct comparison of reverberation-based and stellar dynamical-

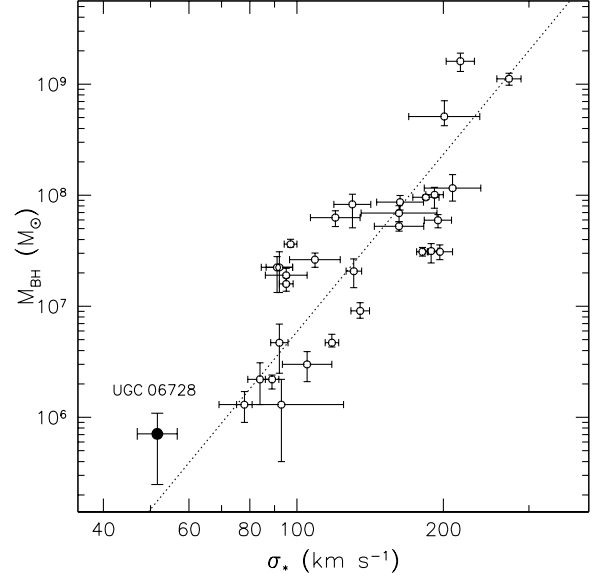


FIG. 10.— UGC 06728 (filled point) and the AGN $M_{\text{BH}} - \sigma_*$ relationship from Grier et al. (2013).

based black hole mass measurements with current and near-future technology, UGC 06728 could potentially be a worthwhile target for dynamical modeling.

6.3. Mass and Spin Implications

Walton et al. (2013) analyzed *Suzaku* observations of UGC 06728 and determined that it was a “bare” AGN, with minimal intrinsic absorption. Fitting the X-ray spectrum with a relativistic reflection model, and assuming an accretion disk inclination of $i = 45^\circ$, they determined a dimensionless spin parameter of $a > 0.7$, indicating the black hole is spinning rapidly. Combined with our mass constraint of $M_{\text{BH}} = (7.1 \pm 4.0) \times 10^5 M_\odot$, UGC 06728 is one of a small number of massive black holes that are completely characterized. A few other low-mass black holes have both mass and spin constraints, and they appear to agree with the properties derived for UGC 06728. MCG-6-30-15 is only slightly more massive with $M_{\text{BH}} = (1.6 \pm 0.4) \times 10^6 M_\odot$ (Bentz et al. 2016) and is spinning near maximally ($a > 0.9$; Brenneman & Reynolds 2006; Chiang & Fabian 2011; Marinucci et al. 2014). NGC 4051 is another example, with $M_{\text{BH}} = (1.3 \pm 0.4) \times 10^6 M_\odot$ (Denney et al. 2009b) and $a > 0.99$ (Patrick et al. 2012).

Black hole evolutionary models have only recently begun to treat black hole spin in addition to mass. Depending on the model, it is not clear if the properties of the black hole in UGC 06728 are expected or surprising. For example, the model of Volonteri et al. (2013) predicts that black holes with $M_{\text{BH}} \approx 10^6 M_\odot$ in gas-rich galaxies at $z < 0.5$ (including AGNs) should have slowly rotating black holes with dimensionless spin parameters of $a < 0.4$. This model is based on many observational constraints, including the $M_{\text{BH}} - \sigma_*$ relationship, with which we have shown UGC 06728 to be in agreement. One caveat to the evolutionary model of Volonteri et al. (2013) is that it does not account for black hole feeding through disk instabilities, which could be a reason for the apparent discrepancy here. Disk instability accretion events would likely be correlated and serve to spin up a black hole. The evolutionary models of Sesana et al. (2014) attempt

to include this effect by linking the gas dynamics of the extended galaxy to the central black hole. Their models predict that local black holes with $M_{\text{BH}} \approx 10^6 M_{\odot}$ should tend to be spinning near maximally, and that *accreting* black holes in spiral galaxies should also tend to have near-maximal spins.

Interpretation of black hole spin measurements is still somewhat debated as well. Bonson & Gallo (2016) argue that black hole spins tend to be overestimated in many cases, although they state this is likely not the case for the most maximally spinning black holes ($a > 0.8$). Furthermore, there is a very strong selection bias inherent in the sample of AGNs with spin measurements. Rapidly spinning black holes have significant boosts to their X-ray flux through increased radiative efficiency, and the current sample of AGNs with spin constraints is based on observations of the brightest X-ray sources, so the current sample will strongly favor rapidly spinning black holes (Brenneman et al. 2011; Vasudevan et al. 2016). In any case, UGC 06728 is an important addition to the sample. As the least massive central black hole that has been fully described, it will help to anchor future studies, both observational and theoretical, of central black hole demographics.

7. SUMMARY

We present an $H\beta$ time delay and a reverberation-based black hole mass for the nearby, low-luminosity Seyfert UGC 06728. With $\tau = 1.4 \pm 0.8$ days and $M_{\text{BH}} = (7.1 \pm 4.0) \times$

$10^5 M_{\odot}$, UGC 06728 is at the low end of observed properties within the reverberation mapping sample. The time delay and estimated AGN luminosity agree with the $R_{\text{BLR}} - L$ relationship for other reverberation-mapped AGNs, and a measurement of $\sigma_* = 51.6 \pm 4.9 \text{ km s}^{-1}$ from long-slit spectroscopy shows that the black hole mass agrees with the AGN $M_{\text{BH}} - \sigma_*$ relationship. With $M_{\text{BH}} < 10^6 M_{\odot}$, UGC 06728 is currently the lowest-mass central black hole that is fully described by both direct mass and spin constraints.

We thank the referee for thoughtful comments that improved the presentation of this paper. MCB gratefully acknowledges support from the NSF through CAREER grant AST-1253702. This research is based on observations obtained with the Apache Point Observatory 3.5-meter telescope, which is owned and operated by the Astrophysical Research Consortium. We heartily thank the staff at APO for all their help with this program. This research has made use of the AAVSO Photometric All-Sky Survey (APASS), funded by the Robert Martin Ayers Sciences Fund. This research has made use of the NASA/IPAC Extragalactic Database (NED) which is operated by the Jet Propulsion Laboratory, California Institute of Technology, under contract with the National Aeronautics and Space Administration and the SIMBAD database, operated at CDS, Strasbourg, France.

REFERENCES

- Alard, C. 2000, *A&AS*, 144, 363
 Alard, C., & Lupton, R. H. 1998, *ApJ*, 503, 325
 Bentz, M. B., Cackett, E. M., Crenshaw, D. M., Horne, K., Street, R., & Ou-Yang, B. 2016, *ApJ*, in press (astro-ph/1608.01229)
 Bentz, M. C., Denney, K. D., Cackett, E. M., et al. 2006a, *ApJ*, 651, 775
 Bentz, M. C., Denney, K. D., Grier, C. J., et al. 2013, *ApJ*, 767, 149
 Bentz, M. C., Horenstein, D., Bazhaw, C., et al. 2014, *ApJ*, 796, 8
 Bentz, M. C., & Katz, S. 2015, *PASP*, 127, 67
 Bentz, M. C., Peterson, B. M., Netzer, H., Pogge, R. W., & Vestergaard, M. 2009, *ApJ*, 697, 160
 Bentz, M. C., Peterson, B. M., Pogge, R. W., Vestergaard, M., & Onken, C. A. 2006b, *ApJ*, 644, 133
 Bentz, M. C., Walsh, J. L., Barth, A. J., et al. 2010, *ApJ*, 716, 993
 Blandford, R. D., & McKee, C. F. 1982, *ApJ*, 255, 419
 Bonson, K., & Gallo, L. C. 2016, *MNRAS*, 458, 1927
 Brenneman, L. W., & Reynolds, C. S. 2006, *ApJ*, 652, 1028
 Brenneman, L. W., Reynolds, C. S., Nowak, M. A., et al. 2011, *ApJ*, 736, 103
 Cappellari, M., & Emsellem, E. 2004, *PASP*, 116, 138
 Chiang, C.-Y., & Fabian, A. C. 2011, *MNRAS*, 414, 2345
 Davies, R. I., Thomas, J., Genzel, R., et al. 2006, *ApJ*, 646, 754
 den Brok, M., Seth, A. C., Barth, A. J., et al. 2015, *ApJ*, 809, 101
 Denney, K. D., Peterson, B. M., Pogge, R. W., et al. 2009a, *ApJ*, 704, L80
 Denney, K. D., Watson, L. C., Peterson, B. M., et al. 2009b, *ApJ*, 702, 1353
 Ferrarese, L., & Ford, H. 2005, *Space Sci. Rev.*, 116, 523
 Ferrarese, L., & Merritt, D. 2000, *ApJ*, 539, L9
 Gaskell, C. M., & Peterson, B. M. 1987, *ApJS*, 65, 1
 Gaskell, C. M., & Sparke, L. S. 1986, *ApJ*, 305, 175
 Gebhardt, K., Bender, R., Bower, G., et al. 2000, *ApJ*, 539, L13
 Genzel, R., Pichon, C., Eckart, A., Gerhard, O. E., & Ott, T. 2000, *MNRAS*, 317, 348
 Ghez, A. M., Morris, M., Becklin, E. E., Tanner, A., & Kremenek, T. 2000, *Nature*, 407, 349
 Ghez, A. M., Salim, S., Weinberg, N. N., et al. 2008, *ApJ*, 689, 1044
 Graham, A. W., Onken, C. A., Athanassoula, E., & Combes, F. 2011, *MNRAS*, 412, 2211
 Greene, J. E., Peng, C. Y., Kim, M., et al. 2010, *ApJ*, 721, 26
 Grier, C. J., Martini, P., Watson, L. C., et al. 2013, *ApJ*, 773, 90
 Gültekin, K., Richstone, D. O., Gebhardt, K., et al. 2009, *ApJ*, 698, 198
 Heckman, T. M., & Best, P. N. 2014, *ARA&A*, 52, 589
 Henden, A., & Munari, U. 2014, *Contributions of the Astronomical Observatory Skalnaté Pleso*, 43, 518
 Hicks, E. K. S., & Malkan, M. A. 2008, *ApJS*, 174, 31
 Kent, S. M. 1985, *ApJS*, 59, 115
 Kinney, A. L., Calzetti, D., Bohlin, R. C., McQuade, K., Storchi-Bergmann, T., & Schmitt, H. R. 1996, *ApJ*, 467, 38
 Kollatschny, W. 2003, *A&A*, 407, 461
 Kormendy, J., & Ho, L. C. 2013, *ARA&A*, 51, 511
 Lasker, R., Greene, J. E., Seth, A., van de Ven, G., Braatz, J. A., Henkel, C., & Lo, K. Y. 2016, *ApJ*, 825, 3
 Magorrian, J., Tremaine, S., Richstone, D., et al. 1998, *AJ*, 115, 2285
 Marinucci, A., Matt, G., Miniutti, G., et al. 2014, *ApJ*, 787, 83
 McConnell, N. J., & Ma, C.-P. 2013, *ApJ*, 764, 184
 Onken, C. A., Ferrarese, L., Merritt, D., Peterson, B. M., Pogge, R. W., Vestergaard, M., & Wandel, A. 2004, *ApJ*, 615, 645
 Onken, C. A., Valluri, M., Brown, J. S., et al. 2014, *ApJ*, 791, 37
 Patrick, A. R., Reeves, J. N., Porquet, D., Markowitz, A. G., Braito, V., & Lobban, A. P. 2012, *MNRAS*, 426, 2522
 Peng, C. Y., Ho, L. C., Impey, C. D., & Rix, H. 2002, *AJ*, 124, 266
 Peng, C. Y., Ho, L. C., Impey, C. D., & Rix, H.-W. 2010, *AJ*, 139, 2097
 Peterson, B. M. 1993, *PASP*, 105, 247
 Peterson, B. M., Bentz, M. C., Desroches, L. B., et al. 2005, *ApJ*, 632, 799
 Peterson, B. M., Ferrarese, L., Gilbert, K. M., et al. 2004, *ApJ*, 613, 682
 Peterson, B. M., Wanders, I., Bertram, R., Hunley, J. F., Pogge, R. W., & Wagner, R. M. 1998a, *ApJ*, 501, 82
 Peterson, B. M., Wanders, I., Horne, K., Collier, S., Alexander, T., Kaspi, S., & Maoz, D. 1998b, *PASP*, 110, 660
 Reynolds, C. S. 2014, *Space Sci. Rev.*, 183, 277
 Schlafly, E. F., & Finkbeiner, D. P. 2011, *ApJ*, 737, 103
 Sesana, A., Barausse, E., Dotti, M., & Rossi, E. M. 2014, *ApJ*, 794, 104
 Siverd, R. J., Beatty, T. G., Pepper, J., et al. 2012, *ApJ*, 761, 123
 van den Bosch, R. 2016, *ApJ*, in press (astro-ph/1606.01246)
 van Groningen, E., & Wanders, I. 1992, *PASP*, 104, 700
 Vasudevan, R. V., Fabian, A. C., Reynolds, C. S., Aird, J., Dauser, T., & Gallo, L. C. 2016, *MNRAS*, 458, 2012
 Volonteri, M., Sikora, M., Lasota, J.-P., & Merloni, A. 2013, *ApJ*, 775, 94
 Walton, D. J., Nardini, E., Fabian, A. C., Gallo, L. C., & Reis, R. C. 2013, *MNRAS*, 428, 2901
 White, R. J., & Peterson, B. M. 1994, *PASP*, 106, 879
 Zibetti, S., Charlot, S., & Rix, H.-W. 2009, *MNRAS*, 400, 1181
 Zu, Y., Kochanek, C. S., & Peterson, B. M. 2011, *ApJ*, 735, 80